

## ***Reprint (R39)***

### ***AOTF Microscope for Imaging with Increased Speed and Spectral Versatility***

*Reprinted with permission by Elliot Wachman, Wen-hua Niu, and Daniel Farkas  
Carnegie-Mellon University*

*September 1997*



ChromoDynamics, Inc. 1195 Airport Rd. # 1, Lakewood, NJ 08701  
Tel: 1 732 730 1877 Fax: 1 732 730 3547 Email: [info@chromodynamics.net](mailto:info@chromodynamics.net)



# AOTF Microscope for Imaging with Increased Speed and Spectral Versatility

Elliot S. Wachman, Wen-hua Niu, and Daniel L. Farkas

Center for Light Microscope Imaging and Biotechnology, Carnegie-Mellon University, Pittsburgh, Pennsylvania 15213 USA

**ABSTRACT** We have developed a new fluorescence microscope that addresses the spectral and speed limitations of current light microscopy instrumentation. In the present device, interference and neutral density filters normally used for fluorescence excitation and detection are replaced by acousto-optic tunable filters (AOTFs). Improvements are described, including the use of a dispersing prism in conjunction with the imaging AOTF and an oblique-illumination excitation scheme, which together enable the AOTF microscope to produce images comparable to those obtained with conventional fluorescence instruments. The superior speed and spectral versatility of the AOTF microscope are demonstrated by a ratio image pair acquired in 3.5 ms and a micro-spectral absorbance measurement of hemoglobin through a cranial window in a living mouse.

## INTRODUCTION

As the number of fluorescent probes has proliferated and interest in millisecond cellular dynamics has increased, a pressing need has developed for a fluorescence microscope that is both spectrally versatile and fast. Liquid crystal tunable filters can provide spectral versatility, but their switching speed is fundamentally limited to  $\sim 50$  ms. Acousto-optic tunable filters, however, used in place of both excitation and emission interference and neutral density filters, can provide continuous solid-state tunability throughout the visible spectrum with variable spectral bandwidths and sub-millisecond switching times. There are three primary reasons why this technology has not been pursued more aggressively for fluorescence microscopy: 1) image quality through AOTFs has historically been poor; 2) out-of-band rejection of an AOTF is typically only  $10^{-2}$  to  $10^{-3}$  relative to the peak transmission; and 3) AOTFs used for fluorescence imaging have substantially reduced light throughput due to their polarization selectivity and their narrow natural spectral bandwidth relative to typical interference filters.

In a previous publication (Wachman et al., 1996), we investigated the mechanisms of AOTF image blur, and demonstrated methods, including appropriate image processing, to reduce blur to diffraction-limited levels. In the present work, we describe a full AOTF microscope that addresses and overcomes in part each of the difficulties described above. We describe the addition of a dispersing prism following the imaging AOTF; this nearly completely compensates for the intrinsic AOTF blur, leading to a diffraction-limited image without the need for postprocessing. We then discuss an oblique illumination system using a

multiline gas laser that compensates for the insufficient background rejection of the AOTF itself. The result is an instrument with image spatial resolution and signal-to-noise comparable to that of a conventional fluorescence microscope. Finally, we demonstrate some of the novel capabilities of the AOTF microscope. We present a ratio image pair acquired in 3.5 ms, highlighting the shuttering and wavelength switching speed of the instrument, as well as *in vivo* spectral images of hemoglobin in mouse cerebral cortical blood vessels, showing the use of the AOTF microscope for microspectrophotometry.

## MATERIALS AND METHODS

### Specimen preparation

The bead sample used for the prism compression data (Fig. 3) consists of  $0.121 \mu\text{m}$  polystyrene beads obtained from Molecular Probes (Eugene, OR). The cells used to demonstrate image resolution with the prism (Fig. 4) and multicolor fluorescence imaging (Fig. 5) are 24-h serum-deprived 3T3 cells fixed in 3.7% formaldehyde and mounted in a glycerol-based medium. Rhodamine phalloidin and Yo-Pro1 used for labeling were also obtained from Molecular Probes. The fast ratio image pair (Fig. 6) uses 200–400-mesh polystyrene beads (Bio-Rad Laboratories, Hercules, CA) transamidated with ethylenediamine for 1 h at  $100^\circ\text{C}$  and then reacted with active esters of Cy3 and Cy5 in bicarbonate buffer. The cyanine dyes used in all experiments were a gift of R. Mujumdar (Carnegie-Mellon University), and are commercially available from Amersham International (Buckinghamshire, England). Details of the mouse preparation (used for Fig. 7) are described in Shonat et al., 1997.

### Microscope system

The various microscope configurations used for the present work are shown schematically in Fig. 1. They will be outlined briefly in the next paragraphs and described in more detail in the body of the paper.

The fluorescence microscope used for all experiments is a Zeiss Axio-plan (Carl Zeiss, Jena, Germany). For excitation of fluorescence using transillumination, we use a Zeiss ultra-darkfield condenser (Model 445315; minimum NA, 1.2; maximum NA, 1.4) and  $40\times$  oil-immersion iris objective (Model 440456; NA variable between 0.7 and 1.3). For the prism experiments, equilateral dispersing prisms made from BK7 (Model 24-3006; Ealing Electro-optics, Holliston, MA) and SF2 flint glass (Model 01

Received for publication 3 February 1997 and in final form 20 May 1997.

Address reprint requests to Dr. Elliot S. Wachman, Carnegie-Mellon University, 4400 5th Ave., STC, Pittsburgh, PA 15213. Tel.: 412-268-7383; Fax: 412-268-1248; E-mail: ew2w@andrew.cmu.edu.

© 1997 by the Biophysical Society

0006-3495/97/09/1215/08 \$2.00

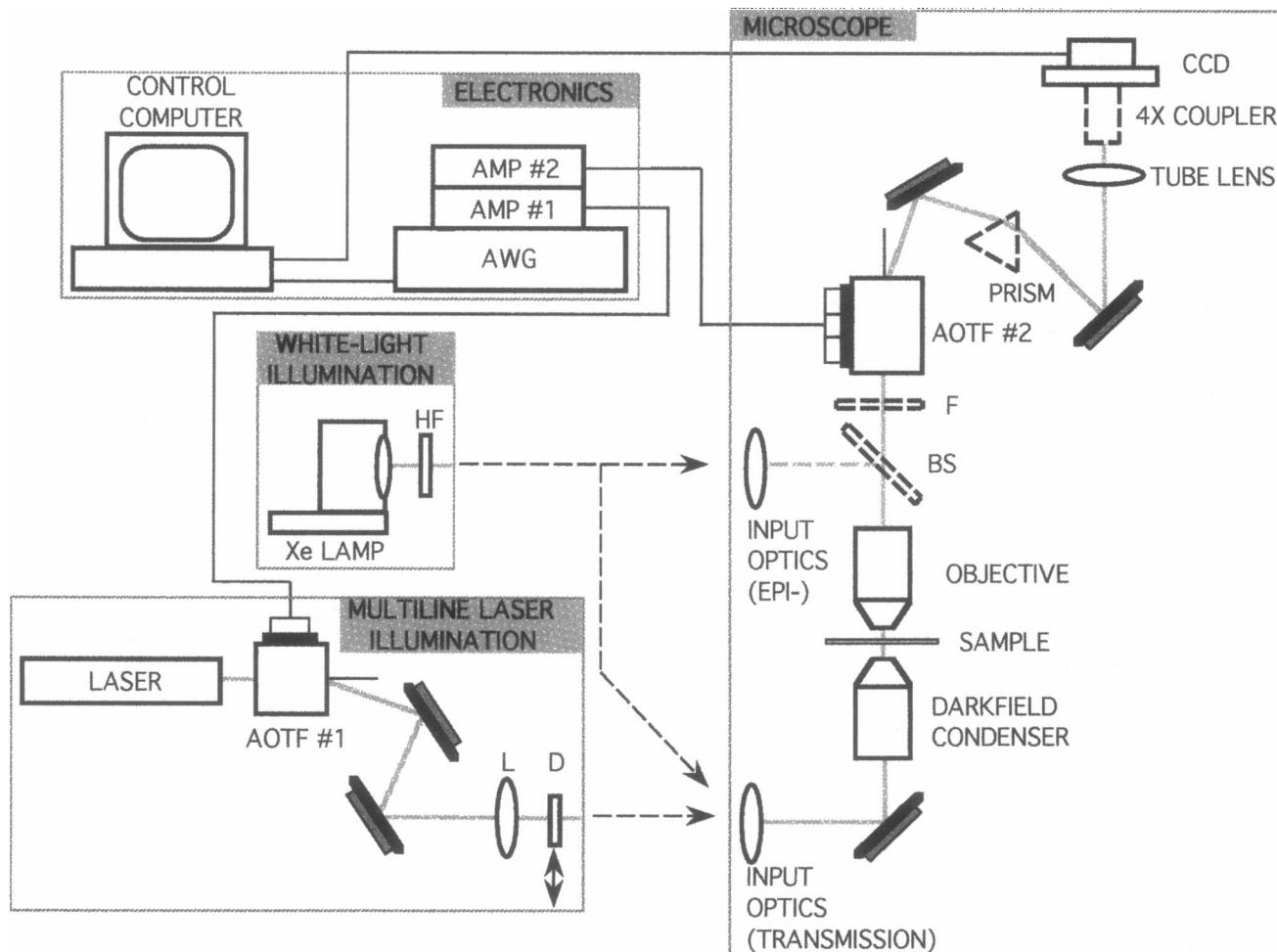


**FIGURE 1** Schematic of the AOTF microscope. Individual lines from an argon-krypton laser are selected by AOTF #1, focussed by a lens (*L*) and made incoherent by a holographic diffuser (*D*) mounted on a small vibrating speaker, to provide oblique excitation via a darkfield condenser; a multiline notch filter (*F*) placed after the sample is used to reject stray light. White-light illumination is provided by a 75-W Xe lamp with heat filter (*HF*) in either epi- (using beam splitter, *BS*) or transmission excitation. Light from the sample is collected by an objective and filtered by AOTF #2, with an equilateral BK7 or SF2 prism used for blur compensation, and sent to a cooled CCD camera. Electronic control is provided by a two-channel RF arbitrary waveform generator (*AWG*) whose outputs are separately amplified and sent to the AOTF crystals. Optics that are removed for certain experiments are indicated by dark dashed lines.

PEH010/066; Melles-Griot, Irvine, CA) are used; for these measurements a 4× coupler (Model 452985; Carl Zeiss) is placed in front of the image detector.

Multiline laser illumination is provided by an argon-krypton gas laser (Model Innova 70 Spectrum; Coherent, Santa Clara, CA), decohered by focussing the beam with lens *L* onto a 60° holographic diffuser, *D* (Model 44-9090; Ealing), mounted on a small vibrating loudspeaker. A matched multiline notch filter, *F*, (Model Quad-M; Chroma Technology, Brattleboro, VT) placed before the detector is used to reject stray laser light. White light illumination is provided by a 75-W Xe lamp (Carl Zeiss) with heat filter, *HF* (Model 417054; Carl Zeiss).

Except for Fig. 6, all images are taken using a Photometrics Model PH220 cooled CCD camera equipped with a Kodak KAF-1400 chip with a 1317 × 1035 array of 6.8 × 6.8 μm pixels (Photometrics, Tucson, AZ) and controlled by a Macintosh Quadra 950 computer. The ratio image of Fig. 6 is taken with a Princeton Instruments Model TE/CCD-512EFT frame-transfer cooled CCD camera, which uses an EEV chip with a 512 × 1024 array of 15 × 15 μm pixels (Princeton Instruments, Trenton, NJ) controlled by a Dell Pentium 590 computer. The spectral image of Fig. 7 is taken with a Zeiss Plan-Neofluar 10× objective (Model 440330; Carl

Zeiss) and a broadband beamsplitter, *BS* (Model XB14-25X36; Omega Optical, Brattleboro, VT), using epi-illumination with the Xe lamp.

### Acousto-optic crystals

Careful crystal design is essential to proper operation of the microscope. The TeO<sub>2</sub> AOTF crystals used here were fabricated according to our proprietary design by NEOS Technologies (Melbourne, FL) and are shown schematically in Fig. 2; the relevant crystal parameters are shown in Table 1. Crystal lengths, *L*, and incidence angles,  $\theta_i$ , for excitation and imaging are chosen by balancing field-of-view, spectral bandwidth, and device efficiency requirements. The acoustic angle,  $\theta_a$ , is chosen to provide operation at the parallel tangent condition (Dixon, 1967). The exit face angle,  $\theta_e$ , is chosen to eliminate shifts of the output diffracted beam with wavelength (Yano and Watanabe, 1976).

The 15-mm excitation AOTF transducer is sectioned into two slices, each with its own electronic input; the 27-mm emission AOTF transducer is sectioned into seven slices with four independent inputs, three ports connected to two slices each, and one connected to a single slice. Radio-

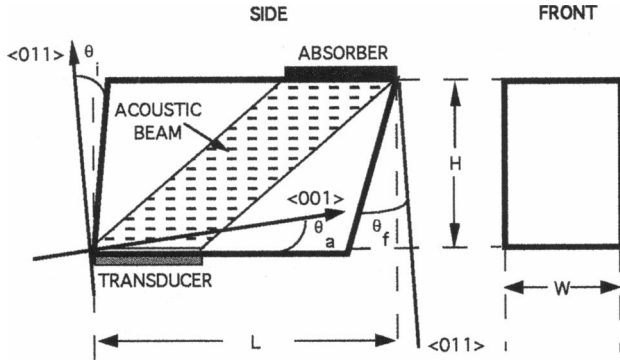


FIGURE 2 Diagram of the AOTF crystals used in the microscope. The input face angle,  $\theta_i$ , acoustic angle,  $\theta_a$ , and exit face angle,  $\theta_f$ , are given relative to the principal axes of the crystal. Values used for the excitation and imaging crystals are shown in Table 1.

frequency (RF) inputs to these ports are produced by a two-channel 400 MHz arbitrary waveform generator, AWG, (Model LW-420; LeCroy, Chestnut Ridge, NY) controlled by a Macintosh Quadra 950 and amplified by two separate high-bandwidth RF amplifiers (NEOS Technologies), as shown in Fig. 1. The excitation AOTF is tunable from 400 to 700 nm, and the imaging AOTF from 450 to 750 nm.

**IMAGE QUALITY**

A traveling ultrasonic wave in an acousto-optic crystal sets up a three-dimensional moving phase diffraction grating for incident light. This acoustic wave may be efficiently generated by applying an RF electronic signal to an acoustic transducer bonded to the crystal surface. Varying the frequency of this RF signal modifies the grating spacing, thereby causing different spectral portions of the incident light to be diffracted. Using multiple RF frequency inputs simultaneously results in a spectral broadening of this diffracted light; changing the amplitude of the RF input(s) alters its intensity. With this electronic control, an acousto-optic crystal can perform as a variable-bandpass, variable-throughput tunable filter as well as a fast light shutter.

Since transducers are of finite length, however, the sound waves they produce in the crystal spread out over a range of angles. A polychromatic optical beam diffracted by these acoustic waves is therefore also angularly spread. This spread occurs in one dimension only, and has a wavelength-dependent magnitude typically  $<1$  mrad, which is determined by the quantity  $d\theta_o/d\lambda$ , where  $\theta_o$  is the output angle of the diffracted beam relative to the  $\langle 011 \rangle$  crystalline axis. A point object viewed through an AOTF using polychromatic light will therefore be blurred in one dimension in the image plane.

Previously, we investigated the relationship between transducer geometry and the angular dependence of the diffracted optical output beam, and demonstrated that this information could be used to correct for image blur through appropriate postprocessing of the AOTF image (Wachman et al., 1996). At objective magnifications of  $100\times$ , the spatial resolution of the processed images was equal to that

of the microscope itself. Here, we approach the same problem by attempting to compensate for the angular spread of the AOTF output beam directly. An AOTF, like a conventional diffraction grating, has a positive dispersion in which red light is diffracted at a greater angle than blue light. A prism, on the other hand, ordinarily has a negative dispersion in which blue light is refracted more than red. In concept, therefore, AOTF image blur should be correctable with a properly designed and oriented dispersing prism. (A similar method of angle compensation has been previously demonstrated in acousto-optic deflectors by Howe et al., 1979.)

In addition to image blur, AOTF imaging crystals also demonstrate image shift, in which the angle of diffraction varies slightly with wavelength. Although this is ordinarily corrected by appropriate cutting of the crystal exit face angle, this technique cannot by itself eliminate image shift once a prism is added. Hence, care must be taken to design a prism/imaging-AOTF-crystal pair for which there is minimal image blur *and* minimal image shift.

We used a simple ray-tracing algorithm to calculate the optimum prism and crystal parameters. First, we calculated the dispersion,  $d\theta_o/d\lambda$ , and output diffraction angle,  $\theta_o$ , of the imaging AOTF with wavelength, and used these values to compute the input angle,  $\theta_{in}$ , at different wavelengths for the prism shown in Fig. 1. In order to minimize image distortion, the prism was oriented with  $\theta_c$  at the center wavelength of interest equal to the prism minimum deviation angle. Since minimum deviation occurs when  $\theta_1 + \theta_2 = \alpha$ , with  $\theta_1, \theta_2$  the internal prism angles and  $\alpha$  the prism apex angle, we may use Snell's law, with  $n$  the index of refraction:

$$\sin \theta_{in} = n \cdot \sin \theta_1$$

$$\sin \theta_o = n \cdot \sin \theta_2$$

to show that the output angle from the prism,  $\theta_o$ , is given by:

$$\theta_o = \sin^{-1}[\sin \alpha \cdot (n^2 - \sin^2 \theta_1)^{1/2} - \cos \alpha \cdot \sin \theta_1]. \quad (1)$$

With this equation, both image shift, arising from the variation of  $\theta_o$  with wavelength, and image blur, arising from a non-zero value of  $d\theta_o/d\lambda$  at a given wavelength, can be evaluated for different choices of AOTF exit face angle, prism composition, and prism apex angle.

Our calculations show that image shift and image blur for a  $\text{TeO}_2$  imaging AOTF can be *simultaneously* best minimized for a prism also fabricated from  $\text{TeO}_2$ . Although other prism materials (BK7, SF2, silica, etc.) can be used to reduce image blur effectively, none of these allow for simultaneous reduction of image shift. In particular, we find that for an imaging AOTF cut with an input face angle,  $\theta_i$ , of  $12^\circ$  such as used in our microscope, minimum image shift and blur result with a  $19^\circ$  apex angle  $\text{TeO}_2$  compensating prism and an AOTF exit face angle measured relative to the  $\langle 011 \rangle$  axis,  $\theta_f$ , of  $-0.7^\circ$ .

**TABLE 1** AOTF Crystal Parameters

Crystal No.	Aperture	$W$	$H$	$L$	$\theta_i$	$\theta_a$	$\theta_f$	Transducer Length	Number of Transducer Ports
1	25 mm	30 mm	27 mm	34 mm	8°	3.95°	10.95°	15 mm	2
2	17 mm	22 mm	22 mm	48 mm	12°	5.95°	16.35°	27 mm	4

Since we did not have an ideal prism/crystal pair, we used the 12°-cut crystal with 16.3° exit face described in Table 1, and off-the-shelf BK7 and SF2 equilateral dispersing prisms (which are calculated to undercompensate and overcompensate, respectively, for the AOTF blur from this crystal) to confirm experimentally the results of our calculations. Previously, we showed that the point-spread-function of an AOTF, corresponding to the intensity profile of an image observed through the crystal of an infinitesimally small bright point, consists of a central peak surrounded by a number of smaller peaks reduced in height by at least an order of magnitude, which result from the angular dispersion of the AOTF output (Wachman et al., 1996). The full angular width at half-maximum (FWHM) of this central peak,  $\Delta\theta_e$ , provides a useful measure of AOTF image blur. With the prism inserted, this FWHM becomes  $\Delta\theta_o$ ; we may therefore define a prism compression ratio equal to the quotient  $\Delta\theta_o/\Delta\theta_e$ . We experimentally measured this ratio with the BK7 prism as a function of wavelength by imaging 0.121  $\mu\text{m}$  (sub-pixel size) polystyrene beads using white-light dark-field illumination with a 4 $\times$  coupler placed before the camera, as shown in Fig. 1. At each wavelength setting of the imaging AOTF, images of the beads were taken both with and without the BK7 prism, and the compression ratio computed from the central-peak widths of their respective intensity profiles. The data, shown in Fig. 3 (*solid squares*), demonstrates that the observed compression agrees both in absolute magnitude and in wavelength dependence with the calculated results (*solid line*).

The compression provided by a standard equilateral SF2 flint glass dispersing prism is significantly greater than that of BK7, and roughly comparable at 600 nm to that provided by the ideal 19° TeO<sub>2</sub> prism described above. To demonstrate the beneficial effect of this compression on image quality we examined actin fibers in 3T3 cells stained with rhodamine phalloidin. We used 514 nm laser excitation and set the emission AOTF for the peak of the fluorescence emission at 580 nm. The imaging AOTF output was passed through the SF2 prism oriented at minimum deviation and sent into the cooled CCD via a 4 $\times$  coupler (Fig. 1).

Fig. 4 shows the results of these measurements. The leftmost image was taken through the AOTF without any compensating prism; resolution is  $\sim 1 \mu\text{m}$  in the direction of AOTF blur, as evidenced in the line profile graph located below the image, and was computed along the white line shown. Using the technique described previously (Wachman et al., 1996), we then experimentally determined a 1-D point-spread-function for the AOTF and used this to numerically deconvolve the effect of AOTF blur on the image.

This processed result is shown in the center of the figure and displays a marked increase in contrast in the blur direction, with some improvement in resolution. The rightmost image is taken through the AOTF using the SF2 prism with no added deconvolution postprocessing. Here the spatial resolution is  $\sim 0.35 \mu\text{m}$ , equivalent to that of the microscope itself, with greatly enhanced contrast. Note in particular the two closely spaced fibers in the center of the line profile, which are clearly observable in the prism image and not evident in the other two images.

This figure demonstrates that the prism-compensated AOTF microscope is capable of an image resolution comparable to that obtained through a conventional microscope even at moderate magnifications and without additional postprocessing. With the addition of a properly designed prism, image blur can no longer be considered an obstacle to using AOTFs for high-resolution microscopy.

### SIGNAL LEVEL AND BACKGROUND REDUCTION CONSIDERATIONS

As discussed, reduced signal levels have long been an obstacle to using AOTFs to image fluorescence. Since an AOTF is polarization-selective, maximum throughputs are

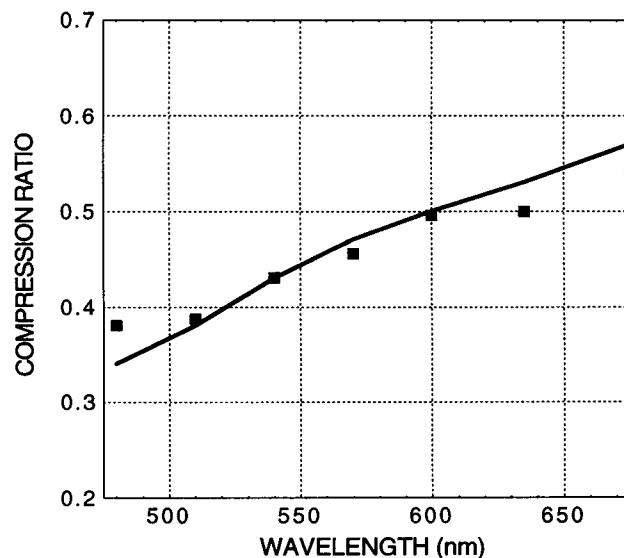
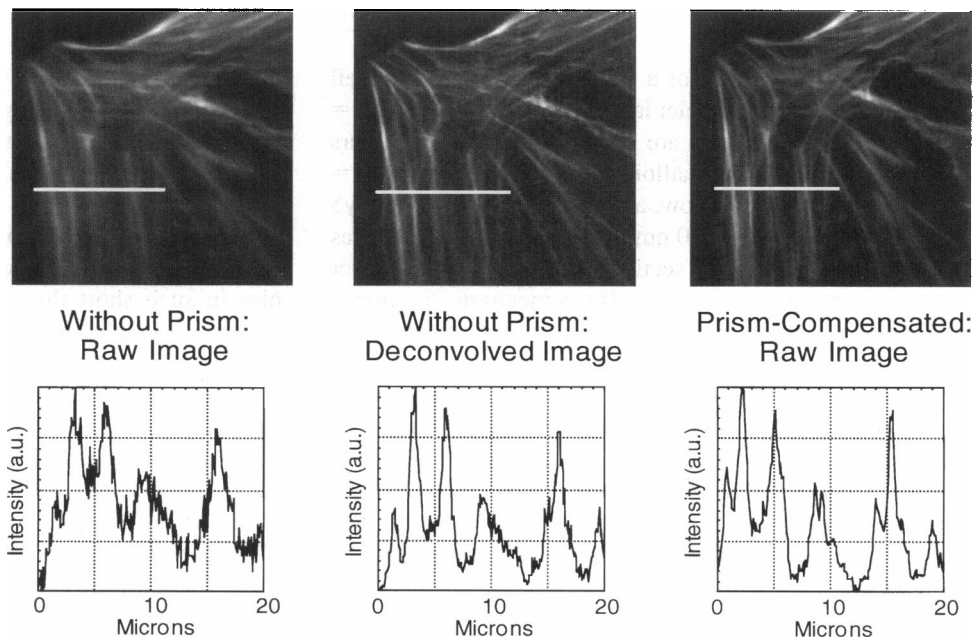


**FIGURE 3** Prism compensation: comparison of measured results with theory. Blur compensation provided by an equilateral BK7 prism, as defined by the compression ratio described in the text, is measured as a function of wavelength (*solid squares*) and compared to values calculated from Eq. 1 (*solid line*).

**FIGURE 4** Prism compensation: actin fibers in fluorescence. Actin fibers in a Swiss 3T3 cell labeled with rhodamine phalloidin are imaged both without (*left and center*) and with (*right*) an equilateral SF2 compensating prism. The center image is digitally processed to remove AOTF blur, as discussed in the text. The graphs below each image correspond to line profile measurements taken along the white lines shown in the pictures. Deconvolution moderately improves image quality, while use of the compensating prism increases both resolution and contrast dramatically. The prism-compensated image displays a spatial resolution at  $40\times$  magnification of  $\sim 0.35\ \mu\text{m}$ , equal to that of the microscope itself.



limited to 50% for unpolarized light. For broad bandwidth inputs such as fluorescence, this throughput is decreased still further due to the roughly 5-nm natural bandwidth of an imaging AOTF. Although both polarizations can be captured and recombined, this technique is only effective in standard filtering applications, as, e.g., with an excitation AOTF; for highest imaging quality through an emission AOTF, only one polarization can be used at a time (Chang, 1992). Losses due to narrow bandwidth can be overcome in part by using multiple, closely spaced RF frequencies to broaden the AOTF bandpass spectrum. One can, in fact, envision using an AOTF in this manner to create a filter with a bandpass electronically customized to match that of the fluorescence signal being measured. We are currently working on refining this technique; at present, overall imaging AOTF throughputs (including polarization losses) of 30% are typical. In many samples, this loss can be partially compensated for without danger of bleaching by a modest increase in the excitation intensity.

The background rejection of AOTFs has also generally been considered inadequate for fluorescence microscopy, since excitation-emission Stokes' shifts of common fluorescent dyes are typically 20 to 40 nm, and AOTFs generally have a transmission roughly  $10^{-2}$  to  $10^{-3}$  of peak at this offset, resulting in a fluorescence signal comparable to the background due to leaked excitation light. Rejection can be improved by using two crystals in series, but on the imaging side this solution is costly (both financially and in light budget) and potentially detrimental to image quality. Alternatively, one could custom-apodize the imaging AOTF transducer to decrease its out-of-band transmission, an option we are currently pursuing.

Another, simpler method to increase AOTF background rejection is to prevent excitation light from ever reaching

the input face of the imaging AOTF. Conventional epi-excitation is undesirable for this purpose, since back-reflections of the excitation light from the microscope objective optics result in prohibitively high background levels when used in conjunction with an imaging AOTF. In addition, epi-fluorescence ordinarily requires the use of a set of custom dichroics, each designed for a specific excitation-emission wavelength pair. The need to mechanically change dichroics in an AOTF microscope would negate any of the superior spectral and speed capabilities of the instrument. We therefore chose to use transmission excitation with oblique sample illumination. Transmission excitation eliminates problematic back-reflections from the objective, obviates the need for a dichroic, and frees up the epi-excitation port for additional measurements. Oblique illumination nearly completely prevents stray excitation light from reaching the imaging AOTF, thereby reducing background levels by several orders of magnitude. When used with a high-power 500-W Xe arc lamp, this illumination scheme results in vastly lower background levels, but is still not sufficient for optimum detection of the weakest fluorescent samples. We are in the process of constructing a new double-AOTF filter for this arc lamp to provide white-light excitation while maintaining minimal background levels.

In the present work, we use a multiline argon-krypton laser tuned by an excitation AOTF together with a multiline notch filter placed after the sample to provide the needed additional background reduction, as shown in Fig. 1. The laser passes through the excitation AOTF and enters the transmission port of our upright microscope. The beam is placed off-axis on a darkfield condenser to provide oblique illumination of the sample, and a  $40\times$  oil-immersion iris objective is used to collect the fluorescence and direct it through the notch filter to the imaging-AOTF/prism com-

bination, with the AOTF-filtered light then sent into the CCD.

Fig. 5 shows an image of a weakly fluorescent 3T3 cell taken with this set-up. Nuclei labeled with Yo-Pro1 ( $\lambda_{\text{exc}} = 488 \text{ nm}$ ,  $\lambda_{\text{em}} = 535 \text{ nm}$ ) are shown in blue, actin fibers labeled with rhodamine phalloidin ( $\lambda_{\text{exc}} = 514 \text{ nm}$ ,  $\lambda_{\text{em}} = 600 \text{ nm}$ ) are shown in yellow, and myosin labeled with Cy5 ( $\lambda_{\text{exc}} = 647 \text{ nm}$ ,  $\lambda_{\text{em}} = 680 \text{ nm}$ ) are shown in red. Since, as discussed in the previous section, the SF2 prism used for these measurements does not fully compensate for image shift with detection wavelength, it was necessary to reregister the individual color images to produce the composite image shown. For the ideal  $\text{TeO}_2$  prism described above, this would not be necessary. The low background and excellent spatial resolution of this multicolor image demonstrate that the AOTF microscope is able to take high-resolution images over a broad tuning range with a signal-to-noise comparable to that obtained with conventional fluorescence microscopes.

## NOVEL CAPABILITIES OF THE AOTF MICROSCOPE

### Increased imaging speed

The results above have demonstrated that the AOTF microscope has an imaging capability on par with other microscopes. The speed and spectral flexibility of the AOTF microscope, however, are far greater than those possible with other instruments. In particular, both the excitation and emission wavelengths can be changed or shuttered on and

off in  $<50 \mu\text{s}$ , a limit given by the acoustic transit time in our somewhat large imaging crystal. This allows investigation of millisecond and sub-millisecond dynamics in living biological systems using multiparameter fluorescence, a capability well beyond the 60-ms minimum wavelength-switching time and 10-ms minimum on-off time of current mechanical filter wheels and shutters. At present, camera sensitivities and probe brightness are not high enough to obtain adequate fluorescence signals from biological samples in such short times. However, as these technologies develop, it will be increasingly possible to exploit the speed of the AOTF microscope.

Millisecond-timescale ratio images are of special interest for many biological measurements (Etter et al., 1996). To demonstrate the capability of the AOTF microscope to take such image pairs, we prepared a sample of polystyrene beads brightly labeled with Cy3, Cy5, and both Cy3 and Cy5, respectively, and used the multiline laser for excitation and a frame-transfer CCD camera with a minimum transfer time of 1.5 ms for detection. The excitation and emission AOTFs were simultaneously gated on for 1 ms in the Cy3 channel (514 nm excitation, 570 nm emission), turned off for 1.5 ms to allow for the frame transfer, and then turned on again for 1 ms in the Cy5 channel (647 nm excitation, 675 nm emission). The resulting images are shown in Fig. 6, with the Cy3 channel displayed in the upper left, the Cy5 channel in the upper right, the composite image in the lower left, and the ratio image in the lower right. This image set, acquired in 3.5 ms (a value limited by the speed of our

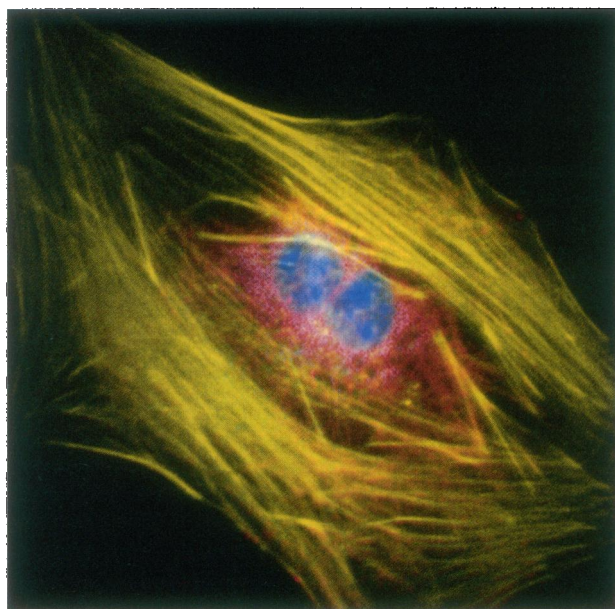


FIGURE 5 Multiwavelength fluorescence imaging with the AOTF microscope. A binucleated Swiss 3T3 cell is shown with nuclei (blue) labeled with Yo-Pro1, actin fibers (yellow) labeled with rhodamine phalloidin, and myosin fibers (red) labeled with Cy5. Image quality is similar to that of a conventional fluorescence microscope.

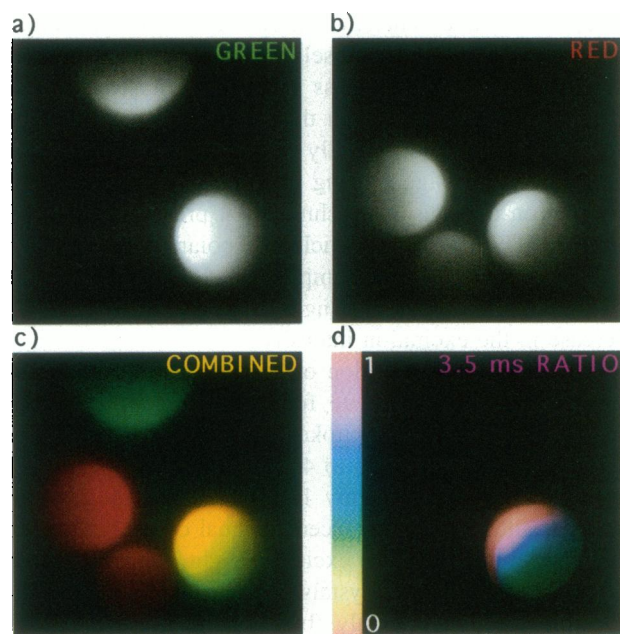


FIGURE 6 Fast ratio imaging: ratio image pair taken in 3.5 ms. A sample containing 200–400-mesh Cy3 (green), Cy5 (red), and doubly labeled Cy3 and Cy5 (yellow) polystyrene beads are imaged through the AOTF microscope using a frame-transfer camera. The Cy3 (a) and Cy5 (b) channels are each acquired in 1 ms. Frame transfer takes 1.5 ms, so that the combined image (c) and ratio image (d) are acquired in only 3.5 ms.

CCD), is, to the best of our knowledge, the fastest 2-D ratio image taken through a fluorescence microscope, and demonstrates convincingly the shuttering and wavelength-switching speed possible with the AOTF microscope.

## 2-D microspectrophotometry

Another novel application of the AOTF microscope is for imaging microspectrophotometry and microspectrofluorimetry. Since the emission AOTF can be continuously tuned from 450 to 750 nm, pixel-by-pixel spectra of the sample under study can be constructed by taking a series of images at different emission wavelengths. One important application of this technique is to the determination of oxygen saturation levels in the blood vessels of a living animal. In particular, since oxy- and deoxyhemoglobin have markedly different absorption spectra, and blood absorption in the 500–600-nm region is nearly completely dominated by hemoglobin, it is possible to determine the relative percentage of each across the sample by analyzing the reflection spectra measured at different locations (Malonek and Grinvald, 1996). Unlike many other microspectrophotometric techniques, the AOTF microscope can take these spectra over the entire two-dimensional field-of-view at one time.

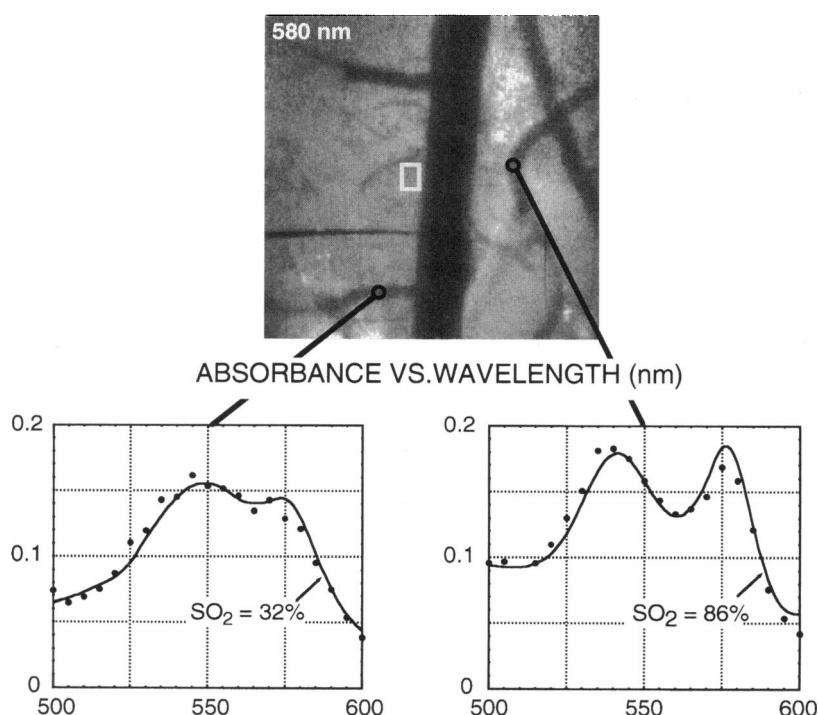
Fig. 7 illustrates results of such a measurement taken on mouse cortical tissue through a cranial window. For this measurement, a Xe lamp was used with a 50-50 beamsplitter for white-light epi-illumination of the tissue using a 10 $\times$  objective. To normalize the reflection data for spectral non-uniformities of the CCD camera, microscope optics, and sub-vasculature tissue reflectivity, we used a spectrum measured from a section of tissue free of large vessels (as, for

example, that enclosed by the white rectangle in the center of the figure). For an evenly illuminated sample, results were largely independent of the specific choice of this background region. A typical reflectance image is shown at the top of the figure, with the corresponding spectra at the two positions indicated displayed in the graphs at the bottom of the figure. In these plots, the normalized spectral data taken through the AOTF (*circles*) is fit (*solid line*) using textbook absorption values for oxy- and deoxyhemoglobin following the method of Malonek and Grinvald, 1996. The agreement is excellent, and the resulting oxygen saturation ( $SO_2$ ) values shown on each graph indicate clearly the substantial difference in oxygenation between the vein on the left and the artery on the right. This information cannot be determined from the intensity image alone.

## CONCLUSIONS

This paper presents a new and powerful tool for biological research: the AOTF microscope. Improvements in excitation optics and the addition of a compensating prism in the imaging path enable the AOTF microscope to take images with a resolution and signal-to-noise comparable to a conventional fluorescence microscope. The AOTF's superior speed and tuning ability open up new possibilities for biological research, including fast dynamics and microspectrophotometry of living systems. Sub-video-rate neural imaging would be an area of particular importance. In addition, the AOTF microscope has the unique ability to take phosphorescence lifetime images in either the time- or the frequency-domain (see Shonat et al., 1997; for background on these techniques see Lakowicz, 1983).

**FIGURE 7** In vivo microspectrophotometry. A reflectance image at 580 nm taken of mouse cortical tissue through a cranial window is shown at the top of the figure. A series of such images at wavelengths between 500 and 600 nm is used to obtain reflectance spectra for each point in the sample by normalizing to a nonvascularized region of tissue, such as shown by the white rectangle in the center of the image. Data for a vein (*left*) and artery (*right*) are shown as solid circles in the graphs at the bottom of the figure. A least-squares fit to these data (*solid line*) yields the oxygen saturation values at each location.



We are currently involved in developing the next-generation AOTF microscope, which will use an arc lamp in place of the laser as an excitation source. This will give the capability for continuous excitation tuning as well as permit use of the important UV-excitable fluorescent probes; the instrument's electronic flexibility will then enable both excitation and emission filter profiles to be customized (Galbraith et al., 1989), leading to a substantial increase in the number of fluorophores that may be used in a multiparameter panel (DeBiasio et al., 1988). Also in progress, as part of our general interest in spectral bio-imaging (Farkas et al., 1996), are experiments using the AOTF microscope for luminescence lifetime-based functional imaging of the mouse brain and spectrally resolved reflection microscopy.

The initial idea of optical compensation for AOTF blur is due to F. Lanni, whose advice throughout this work was invaluable. The cyanine-labeled beads were prepared by B. T. Ballou, computer assistance was provided by C. Lau, and the mouse work was done with the expert collaboration of R. D. Shonat and A. P. Koretsky. Encouragement and support from members of our Center, and particularly D. L. Taylor, are much appreciated.

This research was supported under National Science Foundation Grant MCB 8920118 to our Science and Technology Center, and a grant from the Benjamin Franklin Technology Center of Western Pennsylvania.

## REFERENCES

- Chang, I. C. 1992. Electronically tuned imaging spectrometer using acousto-optic tunable filter. *Proc. SPIE*. 1703:24–29.
- DeBiasio, R. L., L. Wang, G. W. Fisher, and D. L. Taylor. 1988. The dynamic distribution of fluorescent analogues of actin and myosin in protrusions at the leading edge of migrating Swiss 3T3 fibroblasts. *J. Cell Biol.* 107:2631–2645.
- Dixon, R. W. 1967. Acoustic diffraction of light in anisotropic media. *IEEE J. Quant. Elect.* QE-3:85–93.
- Etter, E. F., A. Minta, M. Poenie, and F. S. Fay. 1996. Near-membrane  $[Ca^{+2}]$  transients resolved using the  $Ca^{+2}$  indicator FFP18. *Proc. Natl. Acad. Sci. USA*. 93:5368–5373.
- Farkas, D. L., B. T. Ballou, G. W. Fisher, D. Fishman, Y. Garini, W. Niu, and E. S. Wachman. 1996. Microscopic and mesoscopic spectral bio-imaging. *Proc. SPIE*. 2678:200–209.
- Galbraith, W., L. A. Ernst, D. L. Taylor, and A. S. Waggoner. 1989. Multiparameter fluorescence and selection of optimal filter sets: mathematics and computer program. *Proc. SPIE*. 1063:74–122.
- Howe, D. G., R. N. Blazey, and J. C. Owens. 1979. Optical achromatization for acoustooptic deflectors. U.S. Patent 4,150,880.
- Lakowicz, J. R. 1983. Principles of Fluorescence Spectroscopy. Plenum Press, New York.
- Malonek, D., and A. Grinvald. 1996. Interactions between electrical activity and cortical microcirculation revealed by imaging spectroscopy: implications for functional brain mapping. *Science*. 272:551–554.
- Shonat, R. D., E. S. Wachman, W. Niu, A. P. Koretsky, and D. L. Farkas. 1997. Near-simultaneous hemoglobin saturation and oxygen tension maps in mouse brain using an AOTF microscope. *Biophys. J.* 73:1223–1231.
- Wachman, E. S., W. Niu, and D. L. Farkas. 1996. Imaging acousto-optic tunable filter with 0.35-micrometer spatial resolution. *Appl. Opt.* 35:5220–5226.
- Yano, T., and A. Watanabe. 1976. Acousto-optic  $TeO_2$  tunable filter using far-off-axis anisotropic Bragg diffraction. *Appl. Opt.* 15:2250–2258.